In situ synchrotron X-ray diffraction study of the martensitic transformation in superelastic Ti-24Nb-0.5N and Ti-24Nb-0.5O alloys.

P. Castany, A. Ramarolahy, F. Prima, P. Laheurte, C. Curfs, T. Gloriant

In situ synchrotron X-ray diffraction study of the martensitic transformation in superelastic Ti-24Nb-0.5N and Ti-24Nb-0.5O alloys

P. Castany[1*], A. Ramarolahy[1], F. Prima[2], P. Laheurte[3], C. Curfs[4], T. Gloriant[1]

[1]INSA Rennes, UMR CNRS 6226 ISCR / Chimie-Métallurgie, 20 avenue des Buttes de Coësmes, 35708 Rennes cedex 7, France

[2]Institut de Recherche de Chimie Paris, CNRS UMR 8247– Chimie ParisTech, 11 rue Pierre et Marie Curie, 75005 Paris, France

[3]Université de Metz, UMR CNRS 7239 Laboratoire d'Etude des Microstructures et Mécanique des Matériaux, Ile du Saulcy, 57045 Metz cedex, France

[4]European Synchrotron Radiation Facility (ESRF), 6 rue Jules Horowitz, 38043 Grenoble cedex, France

Abstract:

Mechanisms of superelasticity were investigated by *in situ* cyclic tensile tests performed under synchrotron X-ray radiation on Ti-24Nb-0.5N and Ti-24Nb-0.5O compositions of metastable β titanium alloys. Analyses of diffraction patterns acquired under load and after unloading for each cycle were used to determine the characteristics of the potential mechanisms of deformation in both alloys. The Ti-24Nb-0.5N alloy exhibits a conventional behavior of superelastic β titanium alloys. Synchrotron X-Ray Diffraction (SXRD) experiments proved that superelasticity is exclusively due to the occurrence of a Stress-Induced Martensitic (SIM) transformation from the β phase to the α" phase. The evolution of volume fraction of α" martensite corresponds exactly to the variation of the recovery strain of the cyclic tensile curve. Conversely, the Ti-24Nb-0.5O alloy displays a non-conventional behavior. SXRD experiments showed a huge ability of the β phase to deform elastically until 2.1%. Surprisingly, a reversible SIM transformation also occurs in this alloy but starts after 1% of applied strain that corresponds to the yield point of the stress-strain curve. Although the SIM transformation occurs, the β phase simultaneously continues to deform elastically. The superelasticity of this alloy is unexpectedly due to a combination of a high elastic deformability of the β phase and a reversible SIM transformation. In both alloys, the lattice parameters of the α" martensite evolves similarly in accordance with the initial texture of the β phase and the crystallography of the transformation.

Keywords: titanium alloys; superelasticity; stress induced martensite; *in situ* synchrotron XRD.

* Corresponding author.

E-mail address: philippe.castany@insa-rennes.fr

1. Introduction

Metastable β titanium alloys are currently developed as biomedical Ni-free alloys with shape memory and superelastic properties [1-10]. These specific properties are due to the occurrence of a reversible martensitic transformation from the β parent phase (bcc) to a α" product phase (C-orthorhombic). Among the potential compositions, Ti-Nb based alloys are the most investigated because of the combination of their good biocompatibility and mechanical properties [3-8]. Depending on the Nb content, binary Ti-Nb alloys can display a full α" martensitic microstructure at room temperature and thus exhibit shape memory properties [3,8,11,12]. If the Nb content is higher, the microstructure is fully β at room temperature and the alloys can display a stress-induced martensitic (SIM) transformation leading to superelastic properties [3,5,11]. Addition of ternary or quaternary elements, such as Zr, Sn or Al, can also improve superelasticity [2,13-16]. Particularly, addition of interstitial elements (O or N) allows a strong improvement of both superelastic properties and mechanical strength in binary Ti-Nb based alloys [2,7,17,18] or in more complex Ti-Nb based compositions [19-22].

In superelastic alloys, the study of the SIM transformation is challenging due to its reversibility after the load is released. That is why *in situ* experiments are needed to study the SIM under loading conditions. For example, conventional *in situ* X-Ray diffraction (XRD) studies were performed on binary Ti-26Nb or Ti-13Nb-4Mo alloys (at.%) and allowed to detect the apparition of the α" SIM under loading conditions [5,23,24]. The α" phase is shown to be formed from 0.2% until 2.5% of strain and to be partially reversible after unloading from 2.5% of strain [5,23]. But these experiments were performed only until a deformation of 2.5% followed by an unique unloading, whereas several cycles of loading-unloading until several percent of deformation would allow to obtain a better preciseness on the characteristics of the SIM transformation: strain values at which the transformation starts and finishes to operate, domain of reversibility of the transformation, domains of existence of other mechanisms of deformation such as elasticity or mechanisms of plasticity, etc. However, the main peaks of β and α" phases are difficult to separate because of the relatively great wavelength and the presence of both $K_{\alpha 1}$ and $K_{\alpha 2}$ wavelengths of X-ray sources used in laboratories. In order to avoid these limitations, the use of synchrotron X-ray radiation was also used because of the combination of a shorter wavelength and a better monochromaticity. Synchrotron X-Ray diffraction (SXRD) was especially used for *in situ* experiments on oxygen-added alloys such as Gum Metals [25,26], Ti2448 [22] or TiNbTaZr-based alloys [27]. But, the volume fraction of SIM α" was generally very low because other mechanisms of superelasticity can take place in these alloys due to the presence of oxygen that is known to inhibit the formation of α" [18,20,22]. SXRD was thus never used to study the SIM transformation in alloys of which superelasticity is predominantly due to this mechanism.

This paper focus on two Ti-24Nb based compositions (at.%) alloyed with 0.5% of nitrogen and oxygen, respectively. Their microstructure and mechanical properties have been investigated previously and both alloys exhibit superelastic properties [7]. The nitrogen-added alloy presents a classical behavior with a superelasticity that seems due to SIM α" transformation and the oxygen-added alloy presents the specific features of oxygen-added

alloys. The main objective of this study is thus to investigate the mechanisms of superelasticity of these alloys by *in situ* Synchrotron X-Ray Diffraction (SXRD) analyses during cyclic loading-unloading tensile tests. Special attention is focused on the role of O and N addition on superelastic properties and domains of occurrence of the different mechanisms of deformation that are evidenced.

2. Materials and methods

Both Ti-24Nb-0.5O and Ti-24Nb-0.5N alloys (at.%) were synthesized by cold crucible levitation melting technique (CCLM). For the elaboration, ultra-pure raw metals: 99.999% pure titanium and 99.9% pure niobium were used. Oxygen and nitrogen were added by using 99.8% pure TiO_2 powder and 99.5% pure TiN powder, respectively. Ingots were next homogenized at 1223K during 72ks under high vacuum, followed by water quenching. A cold rolling at room temperature was then applied until 90% of reduction in thickness. Tensile specimens were machined in cold-rolled sheets with normalized shapes: 3 mm width, 0.5 mm in thickness and a gage length of 15 mm. Specimens were finally solution-treated in the β-phase domain at 1123K during 1.8ks under high vacuum and water quenched in order to restore a fully recrystallized microstructure from the cold-rolled state.
After this whole thermo-mechanical process, the microstructure consists of β phase only (bcc structure). More details on microstructure and mechanical properties of these alloys can be found in a previous work [7].
Texture of the β phase was preliminarily measured from conventional X-ray diffraction on a Philips PW3710 system using Cu-Kα1 radiation (λ = 0.154060 nm). Poles figures were then plotted from calculated orientation distribution functions (ODF).
In situ synchrotron X-ray diffraction (SXRD) experiments were carried out at the high-resolution beam line ID31 of the European Synchrotron Radiation Facility (ESRF) in Grenoble (France) using a 0.040002106 nm wavelength radiation. In order to investigate the mechanisms of superelasticity and their reversibility, loading-unloading cycles were performed: the strain was increased by steps of 0.5% until an elongation of 5% and each step was followed by a total release of the stress. Additional cycles were next made until strains of 6%, 8% and 10%. Cyclic tensile tests were performed with a strain rate of 10^{-4} s^{-1} and the tensile direction was chosen parallel to the rolling direction. Diffraction patterns were recorded for each cycle under load and after unloading. The geometry of the set-up is sketched in Fig. 1: tensile specimen and incident beam are fixed whereas the detector moves for 2θ angles from 8° to 26° in order to collect transmitted diffracted beams. Positions of diffraction peaks were then used to identify the presence of different phases and determine their lattice parameters. Intensities of some specific peaks were also used to estimate the relative proportion of different phases.

3. Results

3.1. Initial texture and microstructure

Ti-24Nb-0.5N and Ti-24Nb-0.5O alloys exhibit a microstructure consisting of full β phase equiaxed grains with a typical grain size of about 50 μm and 100 μm, respectively [7]. The smaller grain size in the nitrogen-added alloy is most probably due to a higher β transus temperature than in the oxygen-added alloy because of the stronger α-stabilizing effect of nitrogen [28,29]. Initial crystallographic textures are presented from {110} and {002} poles figures in Fig. 2. Both alloys have the same texture that consists mainly of the {001}<110> component of the α fiber of bcc metals. This texture is more pronounced in the Ti-24Nb-0.5N alloys. This kind of texture is commonly observed in Ti-Nb based titanium alloys after cold-rolling/annealing [30-32] or warm-rolling/annealing thermo-mechanical treatments [33]. Crystallographic calculations have demonstrated that the maximum transformation strain in superelastic β titanium alloys is obtained from the stress-induced martensitic transformation when β grains are orientated with a <110> direction along the tensile direction [31]. This characteristic was also evidenced from experimental studies [30,31,34]. In the present study, tensile specimens are strained along the rolling direction, i.e. along a <110> direction: in turn, if a stress-induced martensitic transformation will occur during tensile tests, the superelasticity will be maximum in both investigated alloys.

3.2. Mechanical properties

Both alloys have an identical high elastic limit value of 665 MPa and Young's moduli of about 50 GPa [7]. It is also worth noting that, for the Ti-24Nb-0.5N alloy, the value of the elastic limit corresponds to the second yield point on the tensile curve, whereas the first yield point at around 130 MPa corresponds to the critical stress to initiate the stress-induced martensitic transformation. The superelasticity, i.e. the total recovery strain, is also similar: 2% for the Ti-24Nb-0.5N alloy and 2.2% for the Ti-24Nb-0.5O alloy [7]. However, cyclic stress-strain curves do not exhibit the same behavior for both alloys (Fig. 3). The Ti-24Nb-0.5N alloy has a "conventional" behavior of superelastic β titanium alloys: a plateau and hysteresis between loading and unloading curves are present (Fig. 3a) that both indicate the existence of a reversible stress-induced martensitic (SIM) transformation. For the Ti-24Nb-0.5O alloy, no plateau is present but hysteresis between loading and unloading curves from 1.5% (Fig. 3b) suggest that such martensitic transformation probably occurs.

3.3. *In situ* synchrotron X-ray diffraction

Fig. 4 displays initial SXRD patterns (top) and final SXRD patterns (bottom) after the entire cyclic tensile test was performed until an elongation of 10% for the Ti-24Nb-0.5N (Fig. 4a) and Ti-24Nb-0.5O alloys (Fig. 4b), respectively. For both alloys, only the $\{110\}_\beta$ peak and the $\{220\}_\beta$ second order diffraction peak are observed before the test, that is in accordance with their strong {*hkl*}<110> texture. Two very small peaks are also detected on both sides

around the $\{110\}_\beta$ peak in the Ti-24Nb-0.5N alloy (Fig. 4a). These peaks correspond to a very small amount of α" martensite, which was formed during the quench. But, as it will be shown further, the presence of this martensite has no effect and can be neglected. These α" peaks are not present in the Ti-24Nb-0.5O alloy because of the stronger inhibitor effect of oxygen on the formation of α" martensite [7]. After being deformed, the α" martensite is the main detected phase for both alloys. The principal detected peaks are indexed in Fig. 4. As the most important peaks are $\{110\}_\beta$, $(020)_{\alpha"}$ and $(002)_{\alpha"}$, the evolution of diffracted peaks of the β and α" phases is more precisely visible on a focus in the 9-10° range during the cyclic tensile test (Fig. 5 and Fig. 6). In order to improve the visibility of the less intense peaks of α" martensite, the first diffractograms are truncated, leading to cut $\{110\}_\beta$ peaks in Fig. 5 and Fig. 6. All entire diffractograms are also given as supplementary materials (Fig. S1 and Fig. S2 for Ti-24Nb-0.5N and Ti-24-Nb-0.5O, respectively).

Fig. 5 shows thus the evolution of most important diffraction peaks during the whole cyclic tensile test on loading (a) and after unloading (b) for each cycle in the Ti-24Nb-0.5N alloy. It can be first noticed that the $\{110\}_\beta$ peak (marked by black triangles) is slightly shifted from its initial position at 0.5% under loading and then remains in the same position by increasing the strain (Fig. 5a). However, its intensity continuously decreases until 3% and disappears at higher strain. At the same time, $(020)_{\alpha"}$ and $(002)_{\alpha"}$ peaks (black squares and black circles, respectively) appears while their intensities are progressively increasing with the strain. It is also worth noting that the peaks due to the very small amount of martensite formed on quenching (open symbols) remains almost at the same position and then vanish: the $(020)_{\alpha"}$ peak (white squares) is at the same position than the $(020)_{\alpha"}$ peak of the stress-induced martensite (black squares) from 1.5% and the $(111)_{\alpha"}$ peak (white stars) disappears from 6% due to its probable reorientation during the plastic deformation. After unloading of each cycle (Fig. 5b), the $\{110\}_\beta$ peak (black triangles) returns at its initial position but is superimposed with the $(002)_{\alpha"}$ peak (black circles) contrarily to what happens under loading where these two peaks are clearly separated. In the strain range of 0-3.5%, the cumulated intensity of $\{110\}_\beta$ and $(002)_{\alpha"}$ peaks after unloading is clearly higher than the intensity of the $\{110\}_\beta$ under loading, what highlights the occurrence of a reversible SIM transformation in the Ti-24Nb-0.5N alloy.

For the Ti-24Nb-0.5O alloy, the evolution of diffraction peaks during the cyclic tensile test is somewhat different (Fig. 6). In the early stage of deformation, the stress-induced martensitic transformation seems not to occur extensively until 1-1.5% on loading (Fig. 6a) whereas the $\{110\}_\beta$ peak (black triangles) continuously shifts to the left instead. From 1.5% to 3%, the $\{110\}_\beta$ peak continues to shift while the $(020)_{\alpha"}$ peak appears (black squares). Moreover, from 3% until the end of the tensile test, the $\{110\}_\beta$ peak disappears and the $(002)_{\alpha"}$ peak of martensite (black circles) appears noticeably. After unloading (Fig. 6b), the $\{110\}_\beta$ peak remains at the same position during the whole cyclic test, suggesting that the shift observed on loading is due to the elasticity of the β phase. Moreover, in the strain range of 1-3.5%, the intensity of this peak is higher after unloading than under loading while inversely the intensity of the $(020)_{\alpha"}$ peak is higher under loading than after unloading, that evidences the occurrence of a reversible stress-induced martensitic transformation for the Ti-24Nb-0.5O

alloy. But this SIM transformation starts to occur at higher applied strain than in the Ti-24Nb-0.5N alloy.

3.4. Lattice parameters

Lattice parameters of β and α" phases were determined from diffraction patterns under loading for both alloys. Their evolution during the whole cyclic tensile test is plotted in Fig. 7, wherein black circles correspond to the Ti-24Nb-0.5N alloy and open circles to the Ti-24Nb-0.5O alloy, respectively.

The lattice parameter of the β phase remains almost constant for the Ti-24Nb-0.5N alloy (black circles); a small increase at the early stage of deformation (from the initial value to 0.5% of strain) can however be observed. On the contrary, the lattice parameter of the β phase in the Ti-24Nb-0.5O alloy is continuously increasing when the strain increases until 2.5% (open circles). After 3% of strain, the β phase is no more detected in diffraction patterns of both alloys and, in turn, lattice parameters cannot be measured any more. It can also be noticed that the initial value of the lattice parameter of the β phase is the same in both alloys and that this value is also constant after unloading during the entire tensile test.

For the stress-induced martensitic α" phase, the evolution of $a_{\alpha"}$, $b_{\alpha"}$ and $c_{\alpha"}$ lattice parameters are similar in both alloys. The $a_{\alpha"}$ and $c_{\alpha"}$ parameters are roughly constant when the strain increases while the $b_{\alpha"}$ parameter continuously increases until 5-6% of strain and remains almost constant at higher applied strain. The elastic deformation of the orthorhombic lattice of α" phase is thus not isotropic in the cell. It is also worth noting that lattice parameters cannot be properly determined for applied strain smaller than 1.5% and 2% for Ti-24Nb-0.5N and Ti-24Nb-0.5O, respectively, due to the too small number of peaks of α" martensite that are detected in diffraction patterns.

4. Discussion

4.1. Evolution of lattice parameters

Evolution of the lattice parameter of the β phase (a_β in Fig. 7) highlights the ability of the β phase to deform elastically in both alloys. For both alloys, the lattice parameter of the β phase after unloading remains constant during the whole cyclic tensile test, proving that the increase of this parameter observed on loading is actually pure elasticity. For the Ti-24Nb-0.5N alloy, this elastic deformation of the β phase only occurs until less than 0.5% of applied strain. Indeed, from 0.5%, the β phase does not deform elastically any more (i.e. its lattice parameter is constant) and the SIM transformation starts to be detected (Fig. 5a). For the Ti-24Nb-0.5O alloy, the β phase deforms elastically until 3% of applied strain. However, the SIM transformation starts from 1% (Fig. 6a) that means SIM transformation and pure elastic deformation of the β phase are operating simultaneously until 3%. From the values of lattice parameters, the maximum elastic distortion of the lattice cell can be easily valuated to 0.07% and 1.5% in Ti-24Nb-0.5N and Ti-24Nb-0.5O, respectively. Theses values correspond to a

maximum lattice strain of 0.1% and 2.1% along the tensile direction (i.e. $<110>_\beta$), respectively: the elastic deformation of the β phase is thus twenty times higher in Ti-24Nb-0.5O than in Ti-24Nb-0.5N, showing the very high ability of the β phase to be deformed elastically in the oxygen-added alloy in comparison with the nitrogen-added alloy.
Conversely, both alloys exhibit a similar evolution of the three lattice parameters of the α" phase that can be explained by considering the crystallography of the SIM transformation. In both alloys, there is the same predominant orientation of β grains (Fig. 2), consisting of a $<110>_\beta$ direction parallel to the rolling direction, i.e. the tensile direction, and a $<100>_\beta$ direction perpendicular to the specimen surface, i.e. parallel to the incident X-ray beam. The stereographic projection of this specific orientation of the β phase is represented in Fig. 8. Application of the α"/β orientation relationship gives 6 equivalent lattice correspondence variants for the martensite from a specific orientation of the β phase [12]. These variants correspond to the different possibilities for which the $[100]_{\alpha"}$ direction coincides with one of the $<100>_\beta$ and both $[010]_{\alpha"}$ and $[001]_{\alpha"}$ coincide with one of the $<110>_\beta$, respectively. However, if the martensite is formed when a uniaxial stress is applied, a variant selection operates: depending on the initial orientation of the β grains, only the variants that are preferentially oriented will be formed [32,35], i.e. the variants that will give a maximum of strain. In the present tested specimens with a $<110>_\beta$ direction along the tensile direction, there is only one correspondence variant that is activated [32,35]. The orientation of the cell axis of this specific variant is reported on the stereographic projection in Fig. 8. For this α" variant, the $a_{\alpha"}$ and $c_{\alpha"}$ axis ($[100]_{\alpha"}$ and $[001]_{\alpha"}$, respectively) are perpendicular to the tensile direction and would thus not evolve when the strain increases. On the contrary, the $b_{\alpha"}$ axis ($[010]_{\alpha"}$) lies along the tensile direction and would be more sensitive to the strain increase. This assumption is in good agreement with the observed evolution of lattice parameters of the α" martensite, where $a_{\alpha"}$ and $c_{\alpha"}$ parameters are almost constant and the $b_{\alpha"}$ parameter increases continuously with the applied strain. The non isotropicity of the elastic deformation of α" phase is thus due to its preferential orientation.

4.2. Evolution of the SIM transformation

In addition to the observation of present peaks on diffractograms, the evolution of the SIM transformation during the cyclic tensile test can be qualitatively illustrated by the evolution of the relative area of the $\{110\}_\beta$ peak (that is the ratio of the current intensity of this peak by the initial intensity of the same peak). The Fig. 9 displays this ratio on loading (squares) and unloading (triangles) for both Ti-24Nb-0.5N (Fig. 9a) and Ti-24Nb-0.5O (Fig. 9b) alloys. In order to compare with the recovery strain, Fig. 9c shows the ratio of recovery strain of both alloys for each cycle defined as:

$$\frac{applied\ strain - residual\ strain}{applied\ strain}$$

For the Ti-24Nb-0.5N alloy, the relative area of the $\{110\}_\beta$ peak on loading starts to decrease from 0.5% of applied strain and continues to decrease strongly until 3.5% (squares in Fig. 9a). At the same time, this area after unloading has a similar behavior (triangles in Fig. 9a) but

with higher values. This behavior illustrates that the volume fraction of the β phase decreases strongly under loading while its volume fraction increases significantly after the load is released. The SIM transformation appears thus to be extensively operating in this 0.5%-3.5% range of applied strain with a high reversibility. By comparing this result with the ratio of recovery strain (black circles in Fig. 9c), one can also remark that the area of the $\{110\}_\beta$ peak and of the recovery strain follow the same evolution: the SIM transformation exhibits the largest reversibility until 2% (ratio of recovery strain higher than 90%) that corresponds to the domain wherein the difference of the relative area of the $\{110\}_\beta$ peak between loading and unloading is the highest; the reversibility decreases further with the applied strain simultaneously with the decrease of the relative area of the $\{110\}_\beta$ peak after unloading. The reversibility of the strain is therefore clearly due to SIM transformation from the β phase to the α" martensite in the Ti-24Nb-0.5N alloy. For applied strain higher than 4%, the relative areas of the $\{110\}_\beta$ peak do not evolve any more: on loading, this peak is no more detected, but its area is not zero after unloading because this β peak is superimposed with the $(002)_{\alpha"}$ peak (unloading only) and its intensity cannot be individually measured after unloading. As a consequence, the constant value of its area from 3.5% indicates just that the reversibility of the SIM transformation does not evolve anymore. Regarding to the relative intensities of $\{110\}_\beta$ and $(002)_{\alpha"}$ peaks on loading, the superimposition of these peaks after unloading has a negligible effect on the evaluation of the relative area of the $\{110\}_\beta$ peak during the first 3% of deformation.

The Ti-24Nb-0.5O alloy exhibits a similar general behavior but with some important differences. First, the relative area of the $\{110\}_\beta$ peak starts to decrease for applied strain higher than 1% (squares in Fig. 9b) and the SIM transformation seems to operate in the 1-3.5% range of applied strain. Secondly, the difference in value of its area between loading and unloading is not so high than in the Ti-24Nb-0.5N alloy, signifying that the SIM transformation has a lesser reversibility in the Ti-24Nb-0.5O alloy. Thirdly, for applied strain higher than 4%, the $\{110\}_\beta$ peak is never superimposed with the $(002)_{\alpha"}$ peak, allowing a precise estimation of the relative area of the single $\{110\}_\beta$ peak after unloading (triangles in Fig. 9b): a part of the SIM transformation is still reversible for applied strain higher than 4% in the Ti-24Nb-0.5O alloy and a residual amount of β phase remains after unloading. In addition, the ratio of recovery strain (open circles in Fig. 9c) shows that the reversibility is total until 1.5% of applied strain. As a consequence, the recovery strain is first only due to the elasticity of the β phase while the SIM transformation starts to operate at around 1-1.5%. The reversibility decreases for applied strain higher than 2% even if the SIM transformation occurs simultaneously with elastic deformation of the β phase. This phenomenon is probably due to the onset of plasticity as the yield stress is reached.

4.3. Correlation between SXRD results and tensile curves

The combination of results about lattice parameters (Fig. 7) and the relative area of the $\{110\}_\beta$ peak (Fig. 9) makes it possible to understand the sequence of activation of each

mechanism in both alloys. This sequence can be summarized on the conventional stress-strain curves of each alloy (Fig. 10).

For the Ti-24Nb-0.5N alloy (Fig. 10a), the elastic deformation of the β phase stops before the 0.5% of applied strain is reached (Fig. 7), that corresponds to the first yielding point. Next, the SIM transformation occurs mainly until about 3.5% of applied strain (Fig. 9), that corresponds to the second yielding point (YS on Fig. 10a). It is also clearly emphasized that the SIM transformation occurs extensively in the 0.5-2.5% range (Fig. 5 and Fig. 9), which corresponds to the stress plateau on the tensile curve (Fig. 10a). For higher applied strain than 3.5%, the SIM transformation stops to occur, except a small amount of reversible transformation, which probably continues to operate (Fig. 9). This domain corresponds thus to the plastic domain wherein dislocation slip and twinning are mainly operating in this alloy [7] and more generally in this alloy family [5,36-38]. As the SIM transformation is not fully reversible from 2% of applied strain (Fig. 9a), one can also supposed that plastic deformation starts to occurs simultaneously with the SIM transformation, even if this former is the main mechanism in the 0.5-3% range of applied strain. This sequence corresponds to what is expected to occur in superelastic metastable β titanium alloys and partially evidenced in previous *in situ* studies [5,23,24].

For the Ti-24Nb-0.5O alloy, the sequence is less conventional (Fig. 10b). The deformation is first only accommodated by the elastic deformation of the β phase until an applied strain value of about 1% (Fig. 7), which corresponds to the part of the cyclic stress-strain curve wherein the loading and unloading curves are exactly superimposed (Fig. 3b) and wherein the slope of the curve is linear. This value is high in comparison with conventional alloys but similar values were already reported in oxygen-added alloys [20,27,39,40]. The most surprising feature is that the SIM transformation starts to operate around 1% of applied strain (Fig. 9) and that this transformation is reversible after unloading while the non-transformed remaining β phase continues to deform elastically under load (Fig. 7). It is also worth noting that the onset of the SIM transformation makes the slope of the tensile curve non-linear (Fig. 3b) as it was already evidenced by Dynamic Mechanical Analysis [32]. Both reversible mechanisms are thus operating simultaneously until approximately 2.5% of applied strain. However, the elasticity of the β phase only occurs in the residual non-transformed β phase that is not the preponderant phase after the SIM transformation started. The SIM transformation continues next until 4% and, finally, after 4%, the deformation is accommodated by the mechanisms of plastic deformation (twinning and dislocation slip [7]). It can also be remarked that no second yielding point is present because the SIM transformation occurs in the “plastic domain” of the stress-strain curve, i.e. the SIM critical stress has a similar value than the critical stress for activation of twinning and dislocation slip. Present *in situ* results shows thus that the yielding point on the curve (YS on Fig. 10b) is due to the beginning of the SIM transformation (and probably also to plastic deformation mechanisms). Plastic deformation mechanisms seems thus to operate simultaneously with the reversible SIM transformation in this alloy. SIM transformation was also already observed in the “plastic domain” in other titanium alloys [41-44]. However, the transformation is not reversible in that case and does not lead to superelasticity, but contributes to high ductility as a TRIP effect (TRansformation-Induced Plasticity) [42,43].

4.4. Effect of oxygen on the SIM transformation

The present study suggests that the superelastic deformation of the Ti-24Nb-0.5O alloy is due to the combination of a wide elastic deformation of the β phase and a reversible SIM transformation. However, other reversible mechanisms are mentioned in the literature for oxygen-added alloy. For example, lattice modulations have been found in Gum metal composition (Ti-23Nb-0.7Ta-1.2O, at.%) [45] and in Ti-23Nb-1O (at.%) alloy [24]. These lattice modulations correspond to nanodomains defined by the relaxation mode of the strain field due to oxygen atoms located in the interstitial sites of the crystal. When a stress is applied, the preferential growth of some pre-existing nanodomains would explain the superelasticity of such alloys, this phenomenon being reversible as demonstrated from *in situ* TEM experiments [24]. The existence of such nanodomains would also inhibit the formation of long-range α" martensite. However, this reversible growth of nanodomains is also characterized by the occurrence of a stress plateau on stress-strain curves and specific peaks of α" seems also not detected from X-ray diffraction under load [24]. As the present Ti-24Nb-0.5O alloy has a lower content of oxygen, does not exhibit stress plateau and clearly present a SIM transformation, this specific mechanism seems not to occur here.
In high oxygen content alloys, a large elasticity of the β phase was sometimes observed from *in situ* laboratory XRD or SXRD experiments. For example, the β phase can be deformed elastically until 1.2% in solution treated Ti-23Nb-0.7Ta-1.2O alloy (at.%, Gum metal composition) [40] or until 1.6% in the Ti-30Nb-10Ta-5Zr alloy (wt.%, with 0.3% of O) [27]. These values are quite smaller, but of the same order of magnitude than the 2.1% of elastic deformation that can be accommodated by the β phase in the Ti-24Nb-0.5O alloy. However, this value of 2.1% is obtained for an applied strain of 2.5%, the rest of deformation being accommodated by the SIM transformation, whereas the elastic deformation in other alloys is smaller. The peculiarity of this alloy is to combine a very high ability of the β phase to be deformed elastically and a reversible SIM transformation, resulting in high superelastic properties coupled with a high yield stress. However, an increase of the O content can suppress totally the SIM transformation and lead to a high recovery strain only due to pure elasticity of the β phase as already evidenced in high oxygen content alloys such as Gum Metals [40].

5. Conclusion

In situ cyclic tensile experiments were performed under synchrotron X-ray radiation on Ti-24Nb-0.5N and Ti-24Nb-0.5O alloys in order to investigate their mechanisms of superelasticity. Both alloys exhibit similar recovery strain but with different behavior: the Ti-24Nb-0.5N alloy presents a classical stress-strain curve with a stress plateau due to a SIM transformation whereas the Ti-24Nb-0.5O alloy does not display such a plateau. Analyses of diffraction patterns acquired under load and after unloading for each cycle allowed to determine precise features and domains of existence of the various mechanisms of deformation:

- For the conventional Ti-24Nb-0.5N alloy, elasticity of the β phase is very limited and the superelasticity is clearly due to the existence of a SIM transformation from the β phase to the α" phase.
- The Ti-24Nb-0.5O alloy exhibits a non-conventional behavior. The β phase has a strong ability to deform elastically until 2.1%. The recovery strain is first only due to elasticity of the β phase until about 1% of applied strain. Between 1 and 2.5% of strain, a SIM transformation occurs simultaneously with elastic deformation of β phase leading to high superelasticity.
- The specific features of the Ti-24Nb-0.5O alloy are due to its intermediate content of O that inhibit not totally the SIM transformation, allowing this transformation to be reversible after the yield point of the tensile curve is reached.
- In both alloys, the elastic deformation of the α" martensite is mainly accommodated by the $b_{\alpha"}$ parameter due to the initial texture of the β phase.

Acknowledgment

This work was supported by the French National Research Agency (N°ANR 08MAPR 0017). We acknowledge the European Synchrotron Radiation Facility for provision of synchrotron radiation facilities (beamline ID31).

References

[1] Niinomi M. Mater Sci Eng A 1998;243:231.
[2] Miyazaki S, Kim HY, Hosoda H. Mater Sci Eng A 2006;438-440:18.
[3] Kim HY, Ikehara Y, Kim JI, Hosoda H, Miyazaki S. Acta Mater 2006;54:2419.
[4] Hao YL, Li SJ, Sun SY, Zheng CY, Yang R. Acta Biomater 2007;3:277.
[5] Tahara M, Kim HY, Hosoda H, Miyazaki S. Acta Mater 2009;57:2461.
[6] Sun F, Hao YL, Nowak S, Gloriant T, Laheurte P, Prima F. J Mech Behav Biomed Mater 2011;4:1864.
[7] Ramarolahy A, Castany P, Prima F, Laheurte P, Péron I, Gloriant T. J Mech Behav Biomed Mater 2012;9:83.
[8] Elmay W, Prima F, Gloriant T, Bolle B, Zhong Y, Patoor E, Laheurte P. J Mech Behav Biomed Mater 2013;18:47.
[9] Abdel-Hady Gepreel M, Niinomi M. J Mech Behav Biomed Mater 2013;20:407.
[10] Bertrand E, Gloriant T, Gordin DM, Vasilescu E, Drob P, Vasilescu C, Drob SI. J Mech Behav Biomed Mater 2010;3:559.
[11] Inamura T, Kim JI, Kim HY, Hosoda H, Wakashima K, Miyazaki S. Philos Mag 2007;87:3325.
[12] Chai YW, Kim HY, Hosoda H, Miyazaki S. Acta Mater 2009;57:4054.
[13] Hao YL, Zhang ZB, Li SJ, Yang R. Acta Mater 2012;60:2169.
[14] Kim JI, Kim HY, Inamura T, Hosoda H, Miyazaki S. Mater Sci Eng A 2005;403:334.
[15] Fukui Y, Inamura T, Hosoda H, Wakashima K, Miyazaki S. Mater Trans 2004;45:1077.

[16] Hao YL, Li SJ, Sun SY, Yang R. Mater Sci Eng A 2006;441:112.
[17] Tahara M, Kim HY, Hosoda H, Miyazaki S. Funct Mater Lett 2009;2:79.
[18] Kim JI, Kim HY, Hosoda H, Miyazaki S. Mater Trans 2005;46:852.
[19] Tahara M, Kim HY, Hosoda H, Nam T-h, Miyazaki S. Mater Sci Eng A 2010;527:6844.
[20] Besse M, Castany P, Gloriant T. Acta Mater 2011;59:5982.
[21] Li SJ, Jia MT, Prima F, Hao YL, Yang R. Scripta Mater 2011;64:1015.
[22] Obbard EG, Hao YL, Talling RJ, Li SJ, Zhang YW, Dye D, Yang R. Acta Mater 2011;59:112.
[23] Al-Zain Y, Kim HY, Koyano T, Hosoda H, Nam TH, Miyazaki S. Acta Mater 2011;59:1464.
[24] Tahara M, Kim HY, Inamura T, Hosoda H, Miyazaki S. Acta Mater 2011;59:6208.
[25] Morris Jr JW, Hanlumyuang Y, Sherburne M, Withey E, Chrzan DC, Kuramoto S, Hayashi Y, Hara M. Acta Mater 2010;58:3271.
[26] Talling RJ, Dashwood RJ, Jackson M, Dye D. Acta Mater 2009;57:1188.
[27] Obbard EG, Hao YL, Akahori T, Talling RJ, Niinomi M, Dye D, Yang R. Acta Mater 2010;58:3557.
[28] Ouchi C, Iizumi H, Mitao S. Mater Sci Eng A 1998;243:186.
[29] Godfrey TMT, Wisbey A, Goodwin PS, Bagnall K, Ward-Close CM. Mater Sci Eng A 2000;282:240.
[30] Inamura T, Kinoshita Y, Kim JI, Kim HY, Hosoda H, Wakashima K, Miyazaki S. Mater Sci Eng A 2006;438–440:865.
[31] Kim HY, Sasaki T, Okutsu K, Kim JI, Inamura T, Hosoda H, Miyazaki S. Acta Mater 2006;54:423.
[32] Bertrand E, Castany P, Gloriant T. Acta Mater 2013;61:511.
[33] Sander B, Raabe D. Mater Sci Eng A 2008;479:236.
[34] Yang Y, Castany P, Cornen M, Thibon I, Prima F, Gloriant T. J Alloys Compd 2014;591:85.
[35] Inamura T, Yamamoto Y, Hosoda H, Kim HY, Miyazaki S. Acta Mater 2010;58:2535.
[36] Castany P, Besse M, Gloriant T. Scripta Mater 2012;66:371.
[37] Bertrand E, Castany P, Péron I, Gloriant T. Scripta Mater 2011;64:1110.
[38] Castany P, Besse M, Gloriant T. Phys Rev B 2011;84:020201.
[39] Hao YL, Li SJ, Sun BB, Sui ML, Yang R. Phys Rev Lett 2007;98:216405.
[40] Kuramoto S, Furuta T, Hwang J, Nishino K, Saito T. Mater Sci Eng A 2006;442:454.
[41] Grosdidier T, Philippe MJ. Mater Sci Eng A 2000;291:218.
[42] Marteleur M, Sun F, Gloriant T, Vermaut P, Jacques PJ, Prima F. Scripta Mater 2012;66:749.
[43] Sun F, Zhang JY, Marteleur M, Gloriant T, Vermaut P, Laillé D, Castany P, Curfs C, Jacques PJ, Prima F. Acta Mater 2013;61:6406.
[44] Farghadany E, Zarei-Hanzaki A, Abedi HR, Dietrich D, Lampke T. Mater Sci Eng A 2014;592:57.
[45] Kim HY, Wei L, Kobayashi S, Tahara M, Miyazaki S. Acta Mater 2013;61:4874.

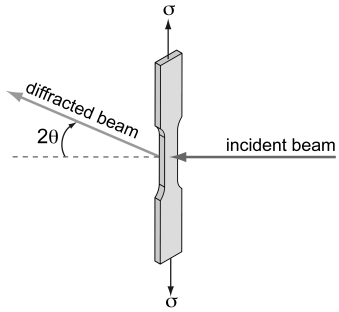

Fig. 1. Schematic drawing of the geometry of the *in situ* SXRD tensile experiment.

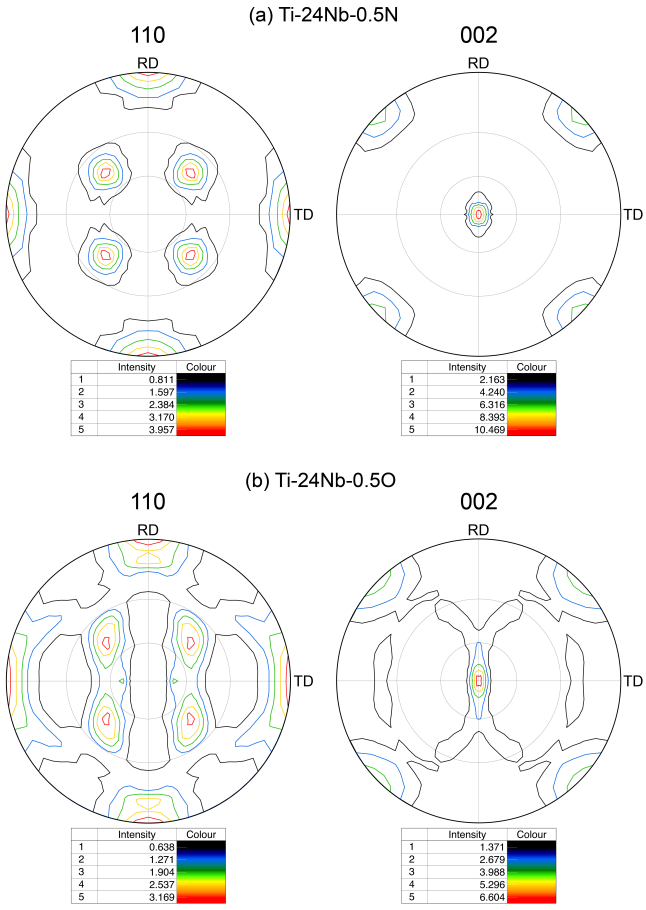

Fig. 2. Calculated {110} and {002} pole figures of the Ti-24Nb-0.5N (a) and Ti24-Nb-0.2O (b) alloys.

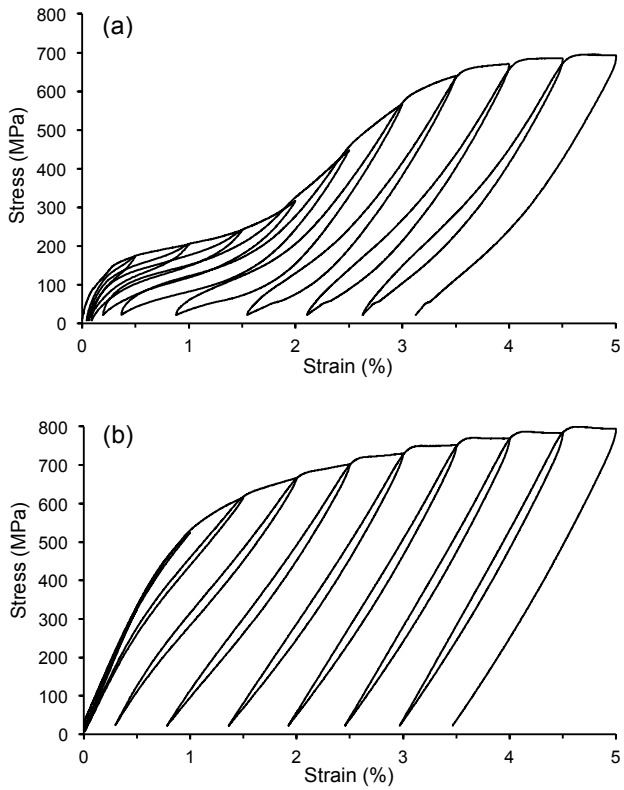

Fig. 3. Cyclic stress-strain curves of the first 5 % of strain of Ti-24Nb-0.5N (a) and Ti24-Nb-0.2O (b) alloys.

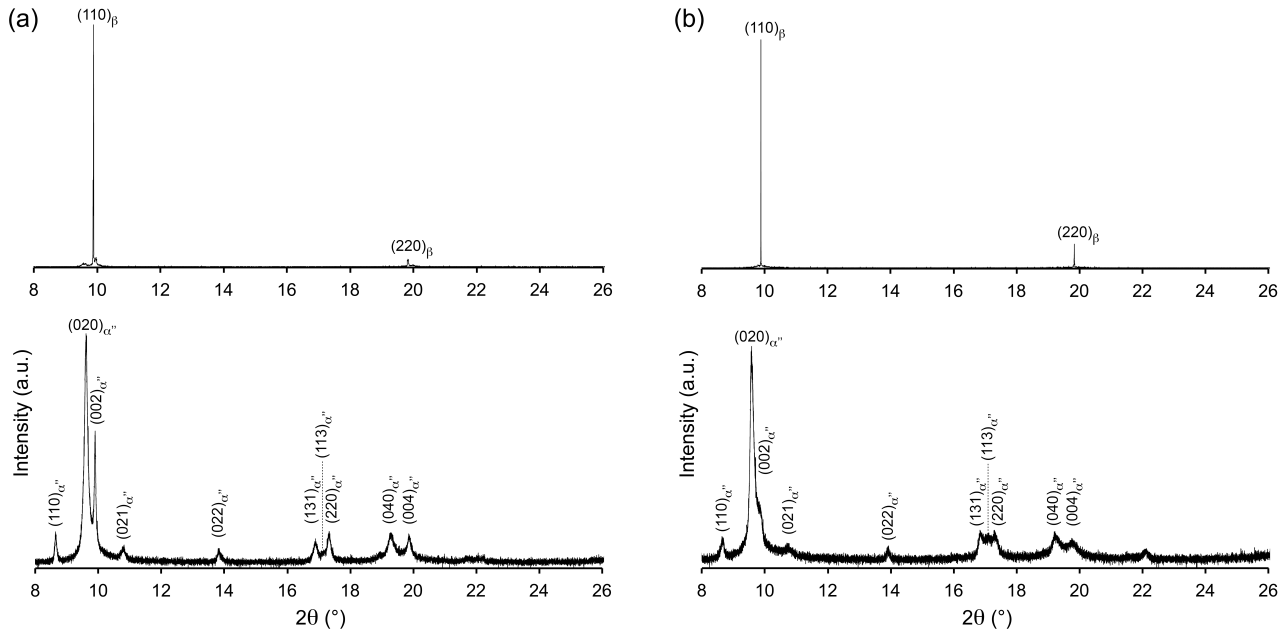

Fig. 4. SXRD patterns acquired before starting the tensile test (top) and after the end of the entire cyclic tensile test (bottom) for Ti-24Nb-0.5N (a) and Ti24-Nb-0.2O (b) alloys.

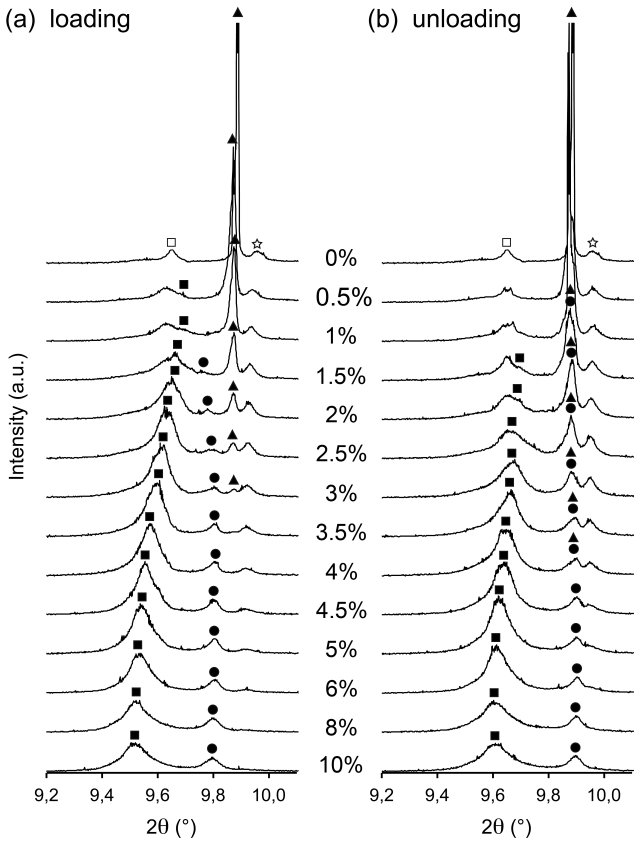

Fig. 5. SXRD patterns zoomed around the $\{110\}_{\beta}$ peak (black triangles) acquired during the *in situ* cyclic tensile test under loading (a) and after unloading (b) for the Ti-24Nb-0.5N alloy; for each cycle, the corresponding strain is indicated beside each pattern. Squared symbols label the $(020)_{\alpha"}$ peaks, circles label the $(002)_{\alpha"}$ peaks and stars label the $(111)_{\alpha"}$ peaks; open symbols correspond to the $\alpha"$ phase formed on quenching.

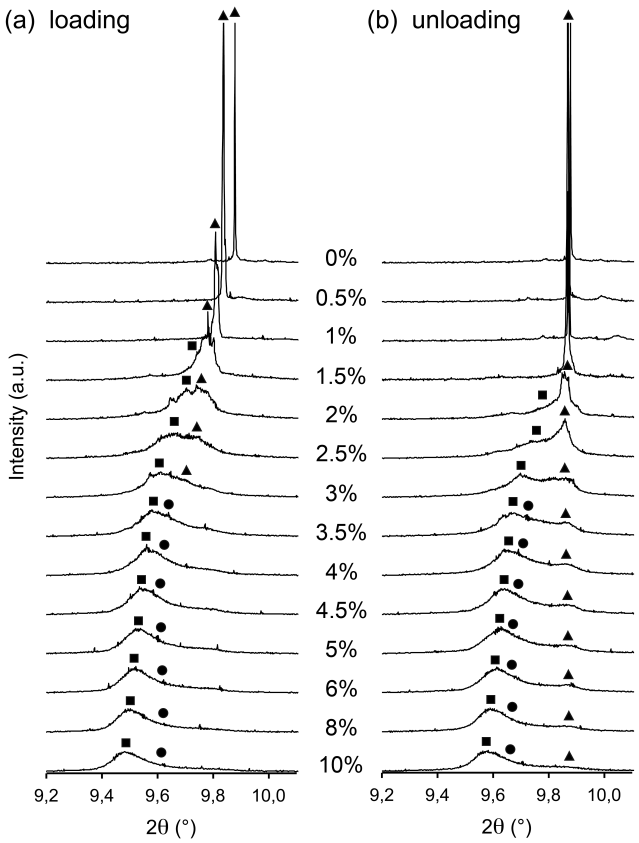

Fig. 6. SXRD patterns zoomed around the $\{110\}_{\beta}$ peak (black triangles) acquired during the *in situ* cyclic tensile test under loading (a) and after unloading (b) for the Ti-24Nb-0.5O alloy; for each cycle, the corresponding strain is indicated beside each pattern; black squared symbols label the $(020)_{\alpha"}$ peaks and black circles label the $(002)_{\alpha"}$ peaks.

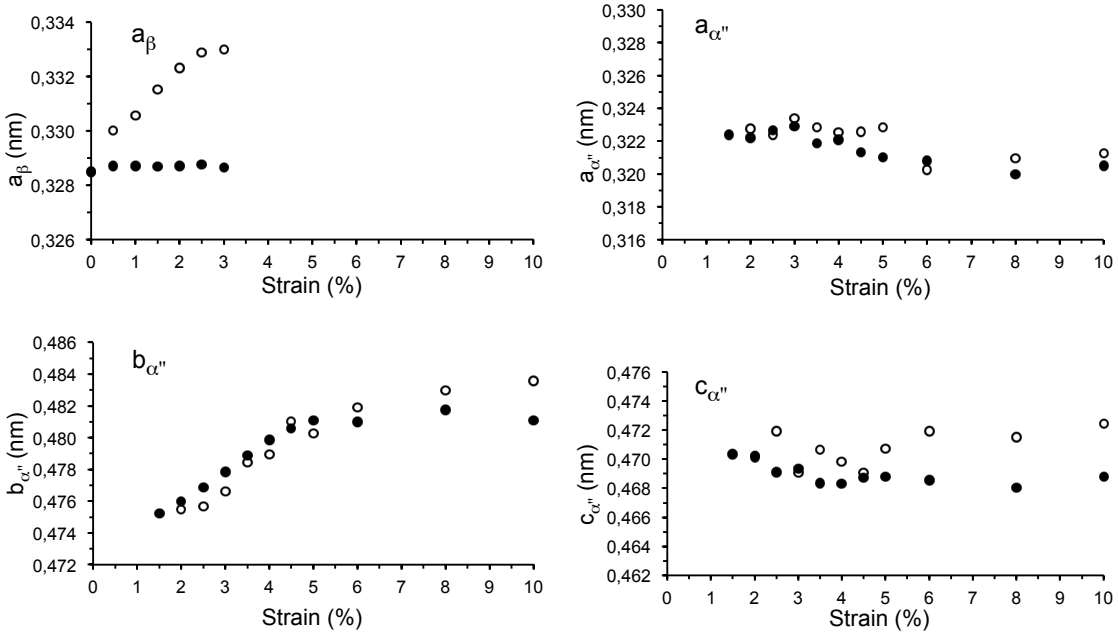

Fig. 7. Evolution of lattice parameters of β and α" phases as a function of strain during *in situ* tensile tests for both Ti-24Nb-0.5N (black circles) and Ti-24Nb-0.5O (open circles).

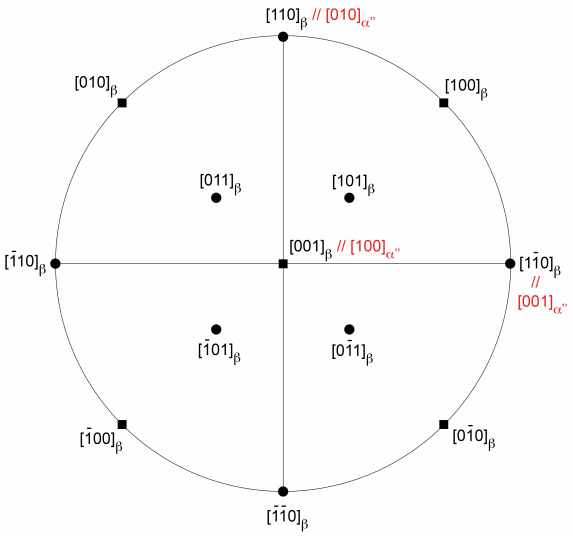

Fig. 8. Stereographic projection of the predominant orientation of β grains in the specimen; the tensile direction is along the $[110]_\beta$ direction ans the X-ray incident beam along the $[001]_\beta$ direction.

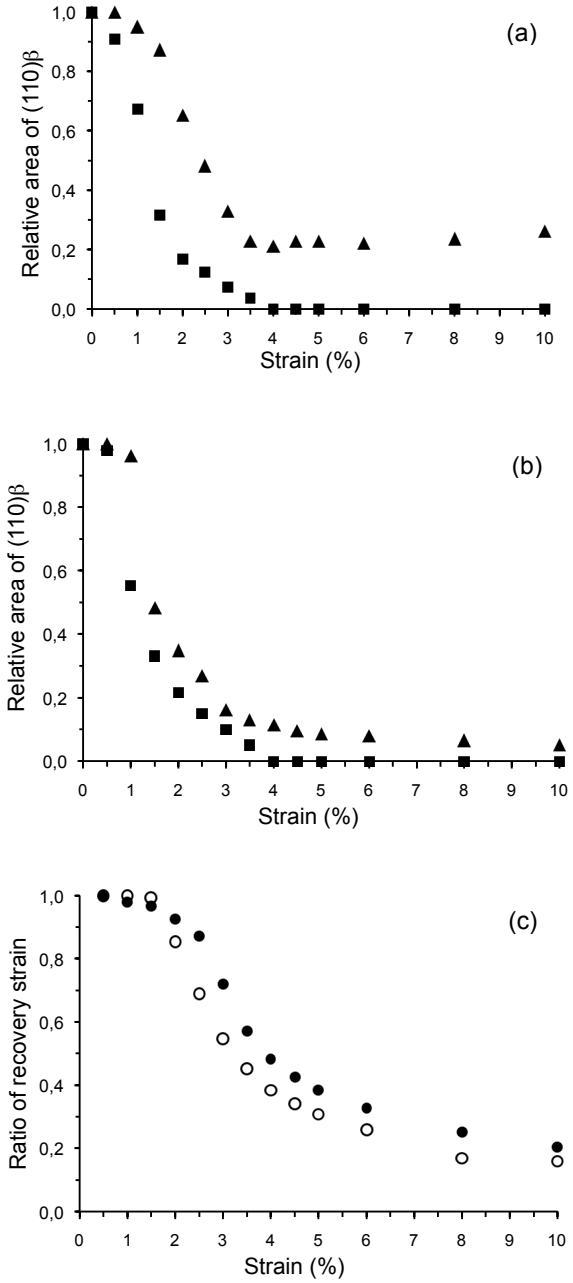

Fig. 9. Evolution of the relative area of the $(110)_\beta$ peak during loading (square) and unloading (triangle) as a function of the applied strain for Ti-24Nb-0.5N alloy (a) and for Ti-24Nb-0.5O alloy (b); evolution of the ratio of recovery strain (c) for both Ti-24Nb-0.5N (black circles) and Ti-24Nb-0.5O (open circles) alloys.

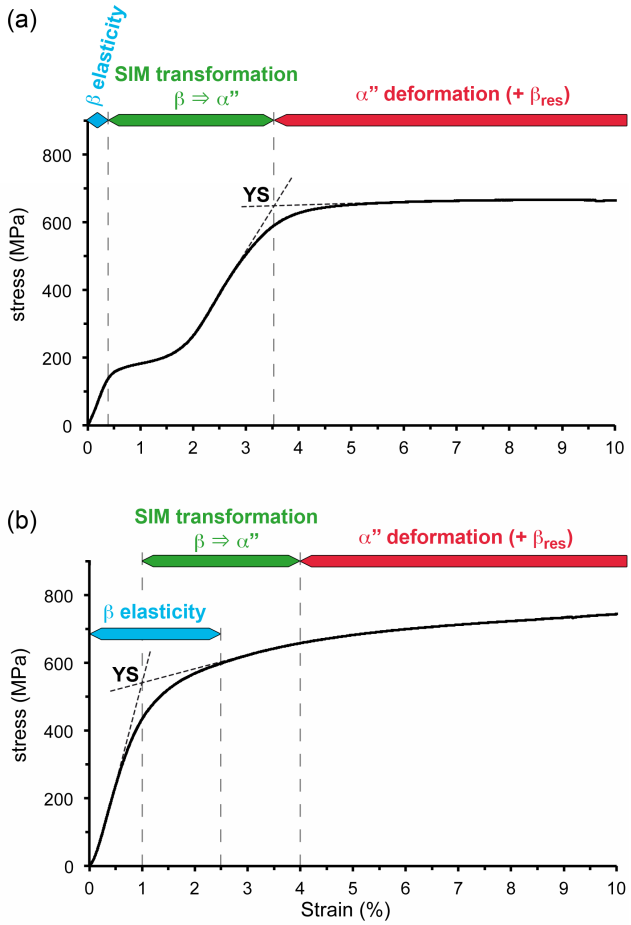

Fig.10. Domains of occurrence of different deformation mechanisms represented on conventional stress-strain curves for Ti-24Nb-0.5N (a) and Ti-24Nb-0.5O (b) alloys; YS indicates the yield stress.

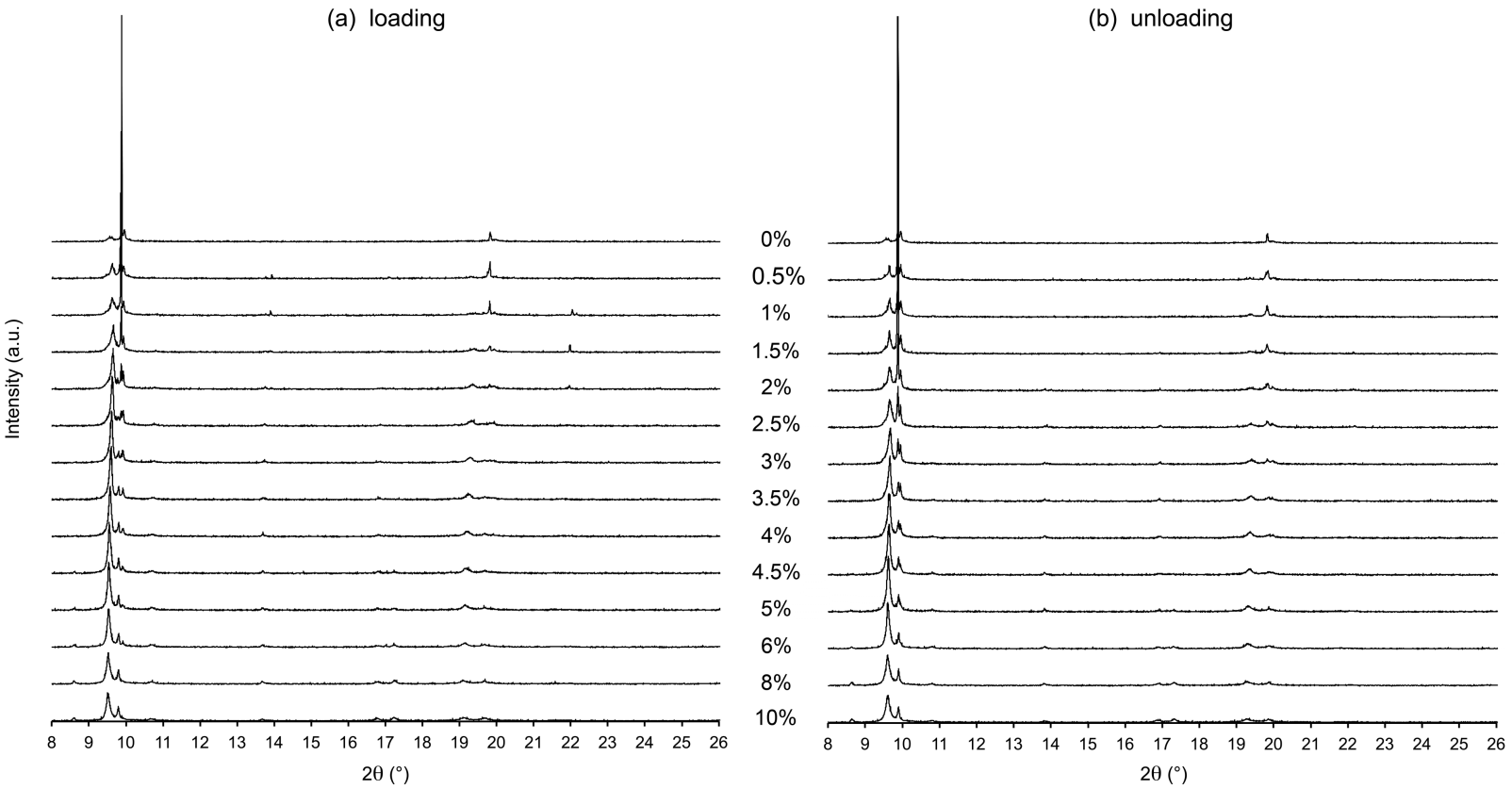

Fig. S1. Whole SXRD patterns acquired during the *in situ* cyclic tensile test under loading (a) and after unloading (b) for the Ti-24Nb-0.5N alloy; the corresponding strain is indicated between the two patterns of each cycle.

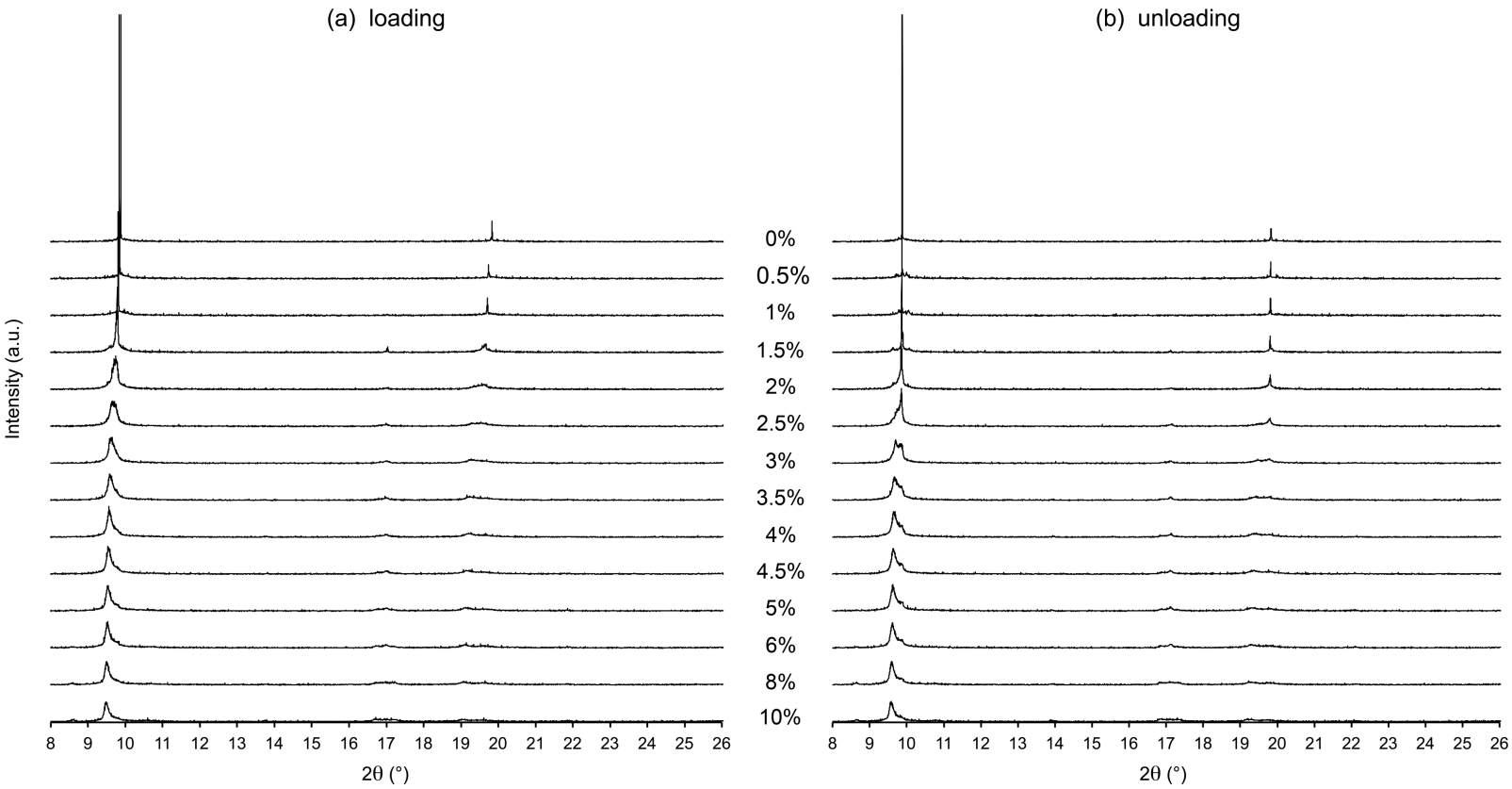

Fig. S1. Whole SXRD patterns acquired during the *in situ* cyclic tensile test under loading (a) and after unloading (b) for the Ti-24Nb-0.5O alloy; the corresponding strain is indicated between the two patterns of each cycle.